

# Effects of metallic system components on marine electromagnetic loop data

Konstantin Reeck<sup>1\*</sup>, Hendrik Müller<sup>2</sup>, Sebastian Hölz<sup>1</sup>, Amir Haroon<sup>1</sup>,  
Katrin Schwalenberg<sup>2</sup> and Marion Jegen<sup>1</sup>

<sup>1</sup>GEOMAR Helmholtz Centre for Ocean Research Kiel, Wischhofstr. 1-3, Kiel, 24148, Germany, and <sup>2</sup>BGR – Federal Institute for Geosciences and Natural Resources Germany, Stilleweg 2, Hannover, 30655, Germany

Received December 2019, revision accepted May 2020

## ABSTRACT

Electromagnetic loop systems rely on the use of non-conductive materials near the sensor to minimize bias effects superimposed on measured data. For marine sensors, rigidity, compactness and ease of platform handling are essential. Thus, commonly a compromise between rigid, cost-effective and non-conductive materials (e.g. stainless steel versus fibreglass composites) needs to be found. For systems dedicated to controlled-source electromagnetic measurements, a spatial separation between critical system components and sensors may be feasible, whereas compact multi-sensor platforms, remotely operated vehicles and autonomous unmanned vehicles require the use of electrically conductive components near the sensor. While data analysis and geological interpretations benefit vastly from each added instrument and multidisciplinary approaches, this introduces a systematic and platform-immanent bias in the measured electromagnetic data. In this scope, we present two comparable case studies targeting loop-source electromagnetic applications in both time and frequency domains: the time-domain system trades the compact design for a clear separation of 15 m between an upper fibreglass frame, holding most critical titanium system components, and a lower frame with its coil and receivers. In case of the frequency-domain profiler, the compact and rigid design is achieved by a circular fibreglass platform, carrying the transmitting and receiving coils, as well as several titanium housings and instruments. In this study, we analyse and quantify the quasi-static influence of conductive objects on time- and frequency-domain coil systems by applying an analytically and experimentally verified 3D finite element model. Moreover, we present calibration and optimization procedures to minimize bias inherent in the measured data. The numerical experiments do not only show the significance of the bias on the inversion results, but also the efficiency of a system calibration against the analytically calculated response of a known environment. The remaining bias after calibration is a time/frequency-dependent function of seafloor conductivity, which doubles the commonly estimated noise floor from 1% to 2%, decreasing the sensitivity and resolution of the devices. By optimizing size and position of critical conductive system components (e.g. titanium housings) and/or modifying the transmitter/receiver geometry, we significantly reduce the effect of this residual bias on the inversion results as demonstrated by 3D

---

\*E-mail: kreeck@geomar.de

modelling. These procedures motivate the opportunity to design dedicated, compact, low-bias platforms and provide a solution for autonomous and remotely steered designs by minimizing their effect on the sensitivity of the controlled-source electromagnetic sensor.

**Key words:** Electromagnetics, Modelling, Numerical study, Signal processing.

## INTRODUCTION

Over the last years, the marine controlled-source electromagnetic method (CSEM) exhibited large steps in the development of new sensor platforms to meet the task of future resource exploration. In comparison to traditional geophysical and geochemical methods, applied to delineate mineralizations along the seafloor, current investigations demand the detection of extinct and buried mineral deposits. The contrast in electrical conductivity between the valuable ores and the surrounding host rock motivated the development of new CSEM devices. Even though von Herzen *et al.* (1996) and Cairns *et al.* (1996) conducted initial studies on electric measurements at the Trans-Atlantic Geotraverse (TAG) hydrothermal mound, it took over 10 years until severe interest in marine, high-grade, polymetallic deposits and their exploration was fuelled by rising resource prices. Kowalczyk (2008) performed first interdisciplinary studies, including bathymetric and magnetic surveys and a remotely operated vehicle (ROV)-based coil experiment, to search for conductive structures at the Solwara 1 hydrothermal field. Swidinsky *et al.* (2012) studied the sensitivity of transient loop sensors for submarine massive sulphide exploration. Since then, several devices have been applied for massive sulphide mapping, including electrical and electromagnetic (EM) dipole systems (e.g. Gehrmann *et al.*, 2019; Ishizu *et al.*, 2019) and horizontal loop systems that offer a small footprint, high vertical resolution and compactness. GEOMAR's MARTEMIS time-domain electromagnetic (TDEM) and the GOLDEN EYE frequency-domain electromagnetic (FDEM) loop system, operated by Germany's Federal Institute for Geosciences and Natural Resources (BGR), have been developed and deployed at various hydrothermal fields. Conductive structures at the TAG and Palinuro Seamount (Hözl *et al.*, 2015) and in the German licence areas were successfully mapped for polymetallic sulphides at the Central Indian Ridge (Schwalenberg *et al.*, 2016; Müller *et al.*, 2018). Sensor operations in mid-ocean ridge settings, at seamounts of complex bathymetry, and under harsh weather conditions, require rigid and compact devices for safe on-board handling and deep-water surveying. However, especially loop-loop EM systems

also rely on a thoughtful construction and design, avoiding the use of electrically conductive materials in proximity of the receiver to prevent bias on the measured data. Thus, a trade-off between rigid, cost-effective and non-conductive materials (e.g. stainless steel versus fibreglass composites) has to be found. In practice, the use of metals such as titanium is inevitable, considering the need of pressure housings for system electronics and additional measuring or observation devices (e.g. conductivity/temperature/depth probes (CTD), magnetometers, altimeters, acoustic positioning, camera systems inertial measurement units (IMU)). A possible approach is therefore to separate system electronics and sensor to a distance where no bias is measurable. By the nature of marine offshore surveys, the time-cost-benefit equation is critical. This favours the development of multi-sensor platforms or steerable ROV/autonomous unmanned vehicle (AUV)-based designs, to refine and complement the measured data set and enhance geological interpretations (Kowalczyk, 2008; Lee *et al.*, 2016; Bloomer *et al.*, 2018). Here, a spatial separation between the transmitter/receiver and the metal components is constrained by the extremely limited space, if not completely unfeasible. Hence, a certain degree of bias is inevitable in these cases, which are relevant to active noise levels recognized by several authors including Nakayama and Saito (2016) and Bloomer *et al.* (2018). A pure mapping approach is therefore a robust and fast way to identify larger conductivity anomalies by analysing relative deviations from the background signal. Yet, this approach does not exploit the full potential of the method, which aims at the inversion of the measured data to derive physical parameter distributions and geological interpretations. This requires sensitive measurements that are capable of delivering reliable, high-quality data sets. This study therefore assesses and quantifies the static effects of critical system components and evaluates their influence on the produced data sets and inversion results for the first time. Two case studies of highly sensitive, marine CSEM systems with (1) time-domain and (2) frequency-domain coil sensors are analysed to quantify their platform-immanent bias and to develop data calibration and system optimization strategies. The numerical calculations, supported by field data, are carried out

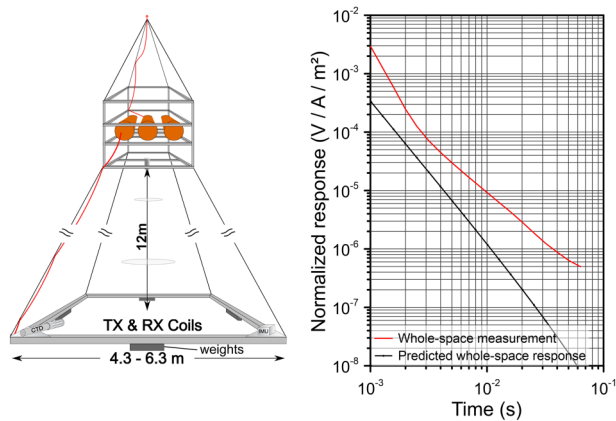


**Figure 1** MARTEMIS TDEM system and (biased) data example: (a) Concept of GEOMAR's MARTEMIS time-domain coil system with separated system electronics (upper frame) and the coincident-loop sensor (lower frame) connected by long ropes. The conductive weights were installed directly onto the coil frame as well as smaller, additional sensors like a CTD and an IMU. (b) Biased data example of a stationary whole-space measurement in the water column during POSS09 in 2017.

by finite element (FE) modelling in the commercially available COMSOL Multiphysics suite, applicable to resolve both time and frequency-domain quasi-static EM problems. The derived bias factors for variable sensor configurations and visualizations based on the computed current density distributions in 3D are especially useful when: (a) developing new or evaluating present CSEM profilers in terms of high sensitivity/low bias, (b) analysing and calibrating existing data sets of other comparable devices to allow for the inversion and full interpretation.

## TIME-DOMAIN SYSTEM

GEOMAR's MARTEMIS system has been under successive development since 2012 and trades a compact design for a distinct separation of up to 15 m between an upper fibreglass frame, holding most electric field distorting titanium, system electronic pressure housings, and a lower frame, carrying a coincident-loop transmitter (TX) and receiver (RX) coil (Fig. 1a). This rope-connected construction allows for a rapid adjustable, modular set-up based on a survey vessel's specification. Usual coil sizes between 18.5 and 39.7 m<sup>2</sup> lead to depth of investigations (DOI) between 30 and 50 m (Hölz *et al.*, 2015). Depending on the target, a horizontal, electrical dipole with two polarizations may be utilized instead of the coil to map resistive structures. Additional instruments, including a conductivity/temperature/depth probe, an IMU and

self-potential (SP) electrodes are usually installed on the coil frame. The instrument is operated at a flight height of 1–3 m above the seafloor which is frequently measured by an altimeter from the upper frame through the coil. Since 2015, several surveys have been carried out on an annual basis, including cruises to the Trans-Atlantic Geotraverse hydrothermal site in 2016, the Mediterranean Palinuro seamount off Sicily in 2015 and 2017 and the Grimsey hydrothermal field in 2018 and 2019 (Hölz *et al.*, 2018). For all cruises, data were successfully recorded, identifying the buried, electrically conductive metal sulphite. Until 2017, metal corner connections and iron weights were utilized as a cheap and durable solution to enhance the rigidity and handling of the coil frame. However, these highly conducting elements also led to a significant, non-uniform and time-dependent offset in the measured data, complicating the analysis substantially (Fig. 1b). This issue is now resolved through improvements on the fibreglass structure and use of non-conducting barite weights. The affected data sets required a thorough post-processing and bias removal prior to the inversion (e.g. Haroon *et al.*, 2018). However, a scientific approval of the used calibration concept has remained pending up to this point and will be demonstrated in the following.

## FREQUENCY-DOMAIN SYSTEM

Federal Institute for Geosciences and Natural Resources' (BGR's) GOLDEN EYE frequency-domain coil system, developed in 2012, features a more compact and rigid design: a fibreglass structure carries the transmitter (TX) and receiver (RX) coils as well as all titanium pressure housings (Fig. 2a). The design enables the device to be used as a multi-sensor platform, incorporating cameras with live link, a conductivity/temperature/depth, a forward-looking sonar, a magnetometer and a self-potential/induced polarization system. The compactness and monitoring capabilities provide the opportunity to easily land the system on the seafloor for stationary, high-resolution measurements. The electromagnetic sensor features a compensation ('bucking') coil that generates a magnetic cavity in place of the RX coil. This allows for sensitive measurements of in-phase and quadrature components while continuously transmitting up to 12 combined sine waves in a frequency range from 10 to 10,000 Hz. The system provides approximately 20 m depth of investigations with high near-surface resolution.

Similar to the MARTEMIS system, a bias was identified in the measured data over all frequencies of the in-phase and quadrature components (Fig. 2b). By submerging

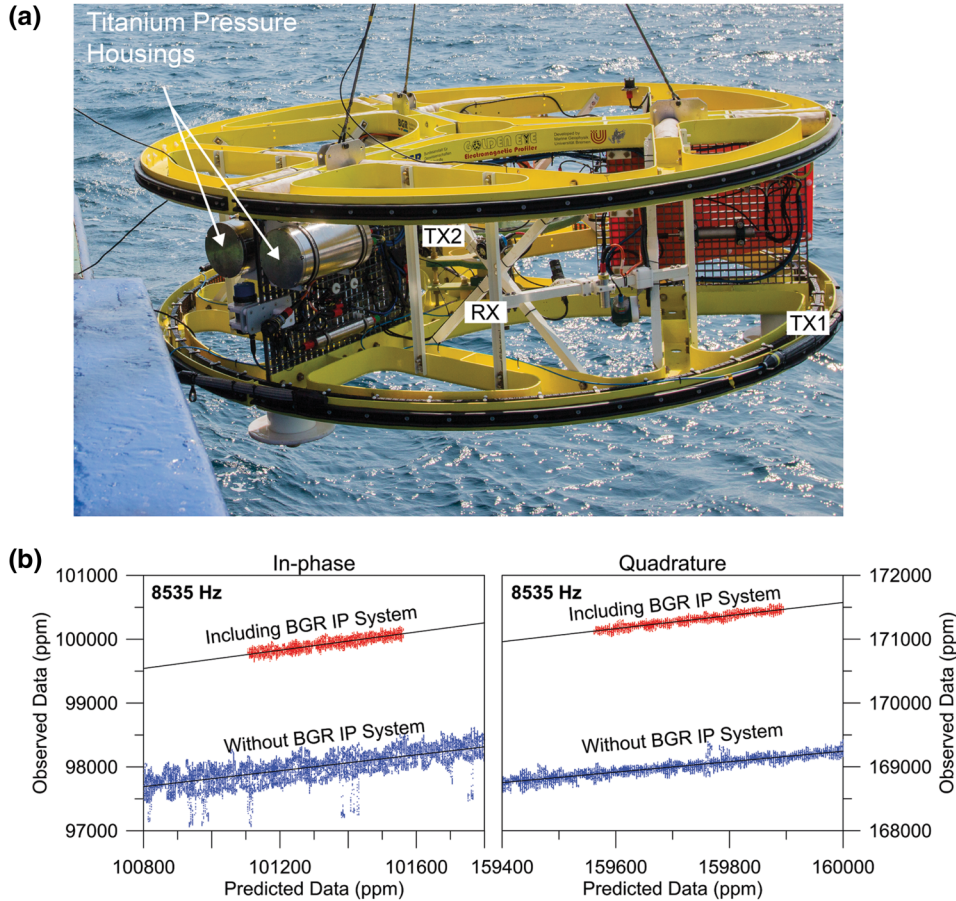


**Figure 2** GOLDEN EYE FDEM system and (biased) data example: (a) GOLDEN EYE profiler deployed from RV Heincke. The FDEM system consists out of a large transmitting (TX1) coil and a coplanar concentric receiving (RX) coil in the lower plane and an upper, elevated ‘bucking’ (TX2) coil in ensemble with an underwater sensing infrastructure. (b) Data example of a range of whole-space measurement in the water column against the predicted responses based on CTD measurements during the INDEX2015 cruise for different setups. The BGR SP/IP system adds two large titanium housings to the instrument that lead to the observed offset (red).

the GOLDEN EYE in a seawater pool with various configurations, it was experimentally proven that the distortions were related to the pressure housings in close proximity of the TX and RX coils. Thus, substantial post-processing and calibration was required to successfully analyse and invert the data sets (Müller *et al.*, 2018). Due to the nature of a compact multi-sensor platform, positioning of pressure housings out of the sensor’s range is not possible. Therefore, efficient calibration methods and system optimization strategies are required to minimize the biasing effects on the data and interpretation.

### FINITE ELEMENT MODELLING IN COMSOL MULTIPHYSICS

The 3D forward modelling was conducted in COMSOL Multiphysics 4.3a and 5.3a using the magnetic fields physics of the

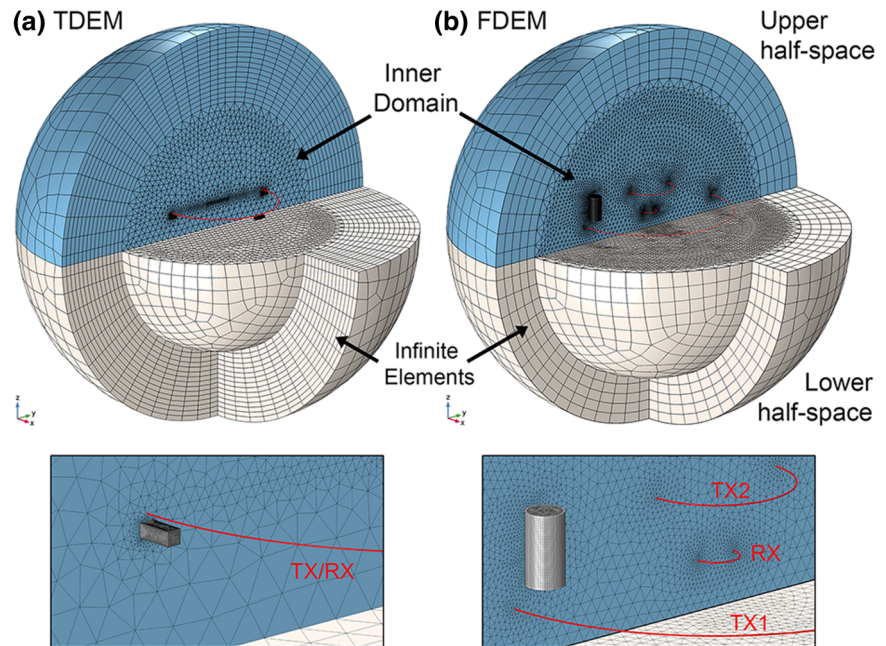
AC/DC module that solves Maxwell-Amperes law (equation (1) for time-domain electromagnetics, respectively, equation (2) for frequency-domain electromagnetics).

$$\nabla \times \mathbf{H} - \sigma \mathbf{E} - \frac{\partial \mathbf{D}}{\partial t} - \mathbf{J}_e = 0, \quad (1)$$

$$\nabla \times \mathbf{H} - \sigma \mathbf{E} - j\omega \mathbf{D} - \mathbf{J}_e = 0, \quad (2)$$

where  $\sigma$  denotes the electric conductivity,  $j$  denotes the imaginary number,  $\mathbf{H}$  denotes the magnetic field,  $\mathbf{E}$  denotes the electric field,  $\mathbf{B}$  denotes the magnetic flux density,  $\mathbf{D}$  denotes the displacement current,  $\omega$  denotes the angular frequency and  $\mathbf{J}_e$  denotes an external current density. Given the constitutive relations for magnetically and electrically linear materials (equations 3 and 4), this transforms into the governing equations (5) and (6) for time and frequency domain that are solved for the

**Figure 3** Finite-element-model set-up for (a) TDEM and (b) FDEM. Cross-section of the finite element models. For the inner computational domain, a tetrahedral meshing is used and refined in areas of high field gradients and low skin depths (e.g. coil area, red). For the outermost area, an infinite elements domain with swept mesh is used, which virtually stretches the coordinates towards infinity and dampens the fields.



magnetic vector potential  $\mathbf{A}$  on a finite element (FE) grid (see COMSOL 2017 for further details).

$$\mathbf{B} = \mu_0 \mu_r \mathbf{H} \quad \text{with} \quad \mu_r = (1 + \chi_m), \quad (3)$$

$$\mathbf{D} = \varepsilon_0 \varepsilon_r \mathbf{E} \quad \text{with} \quad \varepsilon_r = (1 + \chi_e), \quad (4)$$

where  $\mu_0$  and  $\varepsilon_0$  denote the magnetic permeability and electric permittivity of free space,  $\mu_r$  and  $\varepsilon_r$  denote the relative magnetic permeability and electric permittivity, and  $\chi_m$  and  $\chi_e$  the magnetic and electric susceptibility.

$$\sigma \frac{\partial \mathbf{A}}{\partial t} - \varepsilon_0 \varepsilon_r \frac{\partial^2 \mathbf{A}}{\partial t^2} + \nabla \times (\mu_0^{-1} \mu_r^{-1} \nabla \times \mathbf{A}) - \mathbf{J}_e = 0. \quad (5)$$

$$(j\omega\sigma - \omega^2 \varepsilon_0 \varepsilon_r) \mathbf{A} + \nabla \times (\mu_0^{-1} \mu_r^{-1} \nabla \times \mathbf{A}) - \mathbf{J}_e = 0. \quad (6)$$

It is important to note that for the relevant conductivity and frequency range, the quasi-static approximation is assumed so that the corresponding terms of the displacement current in equation (5) and (6) can be neglected.

Initial concepts of the FE models were designed as whole-space and half-space solutions for an efficient, 2.5D axial-symmetric geometry to benchmark and verify the model against analytical solutions and field data with low computational costs. Subsequently, 3D models were developed, incorporating non-symmetric and more complex elements like pressure housings. Different domains are used to apply an ideal, tetrahedral meshing on each component, based on the maxi-

mum skin depth and therefore on the frequency and electrical conductivity of the domain (Fig. 3). A spherical, inner computational domain serves as main model space. In the upper half-sphere, all relevant objects of the device are parameterized, including the transmitter (TX)/receiver (RX) coils as well as weights or pressure housings. The lower half-sphere yields the opportunity to assign a layered earth model and buried objects. Furthermore, a mesh refinement resolves the high field gradients in close proximity of the TX coils. The outer domain is meshed as ‘infinite elements’, used to dampen the fields by virtually stretching the elements to infinity and avoiding any amplifying, diffusion-hindering effects. Prior to the bias modelling, a series of tests were completed to verify the solution’s accuracy. Domain and mesh scaling/sensitivity tests were conducted by analysing the influence of the domain and mesh size.

## TIME-DOMAIN 3D FINITE ELEMENT MODEL AND STUDIES

The upper fibreglass frame of the MARTEMIS system is neglected in the 3D simulations, since experimental field testing showed that the influence of the titanium housings is negligible at a distance of over 15 m from the receiver (RX) coil. This simplifies the model due to the reduced size of the main computational domain and results in significantly less degrees of freedom and computational costs. As a result, the model only

consists of the transmitter (TX) coil, which also acts as a coincident RX (Fig. 3a). For further simplification and symmetry, the coil is chosen to be circular with 4.85 m diameter and 40 A excitation current, reaching the equivalent TX moment of the MARTEMIS' square coil (4.3 m × 4.3 m, 40 A). Due to this simplification, the initially used iron corners were neglected in the model, considering their complex geometry. The modelled bias is solely introduced by the four iron weights. A distance of 1 m to the seafloor is chosen to represent optimal measurement conditions. The induced voltage in the RX coil ( $V_{\text{ind,Rx}}$ ) is subsequently obtained by integrating the time derivative of the vertical magnetic flux density ( $B_z$ ) over the coil area, with  $r$  being the radius and  $\phi$  being the azimuth of the (circular) coil:

$$V_{\text{ind,Rx}} = - \int_0^{r_{\text{Rx}}} \int_0^{2\pi} \frac{dB_z(r, \phi)}{dt} dr d\phi. \quad (7)$$

$V_{\text{ind,Rx}}$  is subsequently normalized by the TX current and coil area.

For the upper half-space, a constant conductivity of 3 S/m was chosen to represent seawater conductivity. A high conductivity of  $10^6$  S/m is assigned to the iron weights, yielding a volume of 4000 cm<sup>3</sup> each. Lower half-space (seafloor) conductivities are varied in a series of studies to simulate low (1 S/m) and high (5 and 10 S/m) conducting half-space and whole-space responses.

Two basic studies were conducted:

1. Whole-space modelling with varying conductivities from 2.5 to 4.5 S/m in steps of 0.5 S/m.
2. Half-space modelling with an upper half-space conductivity of 3 S/m and variable lower half-space conductivities of 1, 5 and 10 S/m.

A time-dependent solver was used in the specified time range from  $10^{-6}$  s to  $10^{-2}$  s, with 10 steps per decade taking an average computational time of 30 min for a half-space model on an Intel i7 8900k with 64 GB of RAM. To stabilize the solutions, the built-in stabilized biconjugate gradient solver was optimized with custom, fixed time-stepping and continuous Jacobian calculations (see COMSOL 2017 for further details). Since instable solutions and aliasing effects can arise from imprecise and automated (free) time-stepping and thus interpolated results of the solver, studies with refined time steps and larger time ranges ( $10^{-9}$  to  $10^0$  s, 20 steps/decade) were carried out to control the solution. These numeric finite element models were compared with results from analytical 1D models.

## FREQUENCY-DOMAIN 3D FINITE ELEMENT MODEL AND STUDIES

The GOLDEN EYE sensor is based on the GEM-3 configuration after Won *et al.* (1997), which is composed of two coaxial, circular transmitting coils. A larger 3.34 m diameter transmitter (TX1) with 60 A (peak–peak) and 8 windings generates the primary magnetic field, while a 1.0 m diameter elevated ‘bucking’ coil (TX2) of 7 reverse windings is tuned to buck out the primary magnetic field at the 0.3 m diameter receiver (RX) coil, located in the centre of the TX1 coil (Figs 2a and 3b). The transmitter (TX) coils are incorporated in the FE model, using line currents. Pressure housings are implemented as cylindrical cavity tubes with corresponding lengths, diameters and wall thicknesses. The conductivity of the titanium cylinders was set to  $4.12 \times 10^6$  S/m. The interior of each pressure tube was chosen to be air to resolve the effect of the pure titanium body. The RX coil is simplified to a point probe, measuring the vertical magnetic flux density at the common centre of TX1 and RX. The response is calculated by the ratio between the un-bucked primary field and the measured, induced secondary field in parts-per-million. For the actual instrument, a small reference coil in the centre of the TX2 coil continuously measures the primary field intensity and is used to normalize the secondary field. Since the induced voltage of a coil is proportional to the time derivative of the orthogonal magnetic flux through the (small) RX coil, a point probe is considered as a suitable simplification. Prior to the model studies, a benchmarking was carried out by comparing the analytical solution to the solution of the point probes and the calculated induced voltage ( $V_{\text{ind,Rx}}$ ) after Ward and Hohmann (1988) from the vertical magnetic flux density ( $B_z$ ) for the RX coil (equation 8) in 2.5D and 3D (Fig. 5):

$$V_{\text{ind,Rx}} = -i\omega \int_0^{r_{\text{Rx}}} \int_0^{2\pi} B_z(r, \phi) dr d\phi. \quad (8)$$

Even though the full modelling of all coils is more elegant, the simplification yields an important time-saving aspect since the degrees of freedom and therefore the computational time of the model are drastically reduced. This enables the model to run in a reasonable amount of time (45 min for a half-space model with full frequency sweep on the Intel i7-8900k with 64 GB of RAM).

The following studies were conducted:

1. Whole-space modelling with varying conductivities from 2 to 4.5 S/m in steps of 0.5 S/m.
2. Half-space modelling with an upper half-space conductivity of 3 S/m and lower half-space conductivities of 0.1, 1, 3, 5 and 10 S/m.

After result evaluation, additional optimization steps were carried out, including the re-dimensioning and repositioning of the pressure housings. For the studies, a common frequency spectrum of the instrument with 30, 105, 285, 885, 2715 and 8535 Hz was swept, according to the set-up of a previous survey. For frequency-domain electromagnetics, the default configuration of the implemented stabilized biconjugated gradient solver was used in all studies.

## RESULTS TIME-DOMAIN

### Verification of 3D finite element model by 1D analytical forward model

A three-dimensional time-domain electromagnetic model of the MARTEMIS system has been developed by using COMSOL's AC/DC magnetic fields module. While first models lacked the precision to match the 1D analytical solution, the customization of the time-stepping solving algorithm solved this issue. Afterwards the model was successfully verified against the 1D analytically calculated forward model (Fig. 4a): the modelled transients for all half-space/whole-space models match the solution of the 1D solution in the analysed time range of  $10^{-5}$  to  $10^{-2}$  s.

### Introduction of the bias effect in 3D finite element model

The reproduction of the bias effect detected in the measured MARTEMIS data sets was achieved by introducing highly conducting ( $10^6$  S/m) iron weights into the 3D model. Figures 4b and c illustrate the difference between biased and unbiased whole-space, respectively, half-space models. A high, but varying deviation of up to 1.5 magnitudes from the original transients (coloured dashed lines) can be observed in the computed time range for both whole-space and half-space models. The separation between the biased and unbiased responses can be observed in early times (between  $10^{-5}$  and  $10^{-4}$  s), and in the same range of time a separation between different half-space models is expected. Since this is one decade below MARTEMIS' earliest sampling time of  $10^{-4}$  s, a recorded transient is likely to be completely biased. The observable variation by the change in seawater conductivity is small due to the generally large amplitude of the bias effect, but becomes more visible at later times ( $10^{-3}$  to  $10^{-2}$  s). In this relevant time range, the different models are well distinguishable, but still biased by a variation of approximately 0.5 S/m at minimum. The biased modelled data correlate well with the biased, measured whole-space data in terms of amplitude and timing

(cf. Fig. 1b). The iron weights are therefore clearly confirmed as a main source of bias, although the amplitude deviation is generally higher in the measured data. This difference is likely due to the neglected iron edges in the modelling and therefore a lower amount of conductive material in the sensor's vicinity. However, the highest amplitude deviations occur at early times, indicating the close proximity of the metal objects to the coil. Further amplitude variations are caused by the secondary electric fields produced through the decaying charge in the conductive weights. Therefore, the bias can be directly related to the change of the induced current density  $J$  in the specified volume of the weights (equation (9)).

$$J = \sigma E. \quad (9)$$

For the background model (volume being water), the induced current density depends on the lower half-space's conductivity (Fig. 4d, coloured lines). By changing the material to iron, the current density increases drastically, leading to an apparent decoupling from the lower half-space's conductivity: a dependency between lower half-space conductivity and induced current density is no longer visible and the resulting calibration offset can be considered nearly static for the analysed range of 1 to 10 S/m (Fig. 4d, black line).

### Calibration of biased data by 1D analytical forward model

The independence from the sub-surface conductivity structure offers the possibility to calibrate the sensor against a known whole-space conductivity model based on measured conductivity/temperature/depth values. However, this approximation can only be considered valid while the apparent decoupling between seafloor and the biasing object holds true, for example, the conductivity contrast stays sufficiently large. A proof of this concept can be presented by calibrating biased data. To avoid further error sources found commonly in measured data sets, synthetic data for whole-space and half-space models are used.

A whole-space model is used as calibration measurement, assuming a steady seawater conductivity of 3 S/m. The 'seafloor measurements' models consist of the upper half-space with a seawater conductivity of 3 S/m and a lower half-space with either 1, 5 or 10 S/m. These are considered as cases of low conducting background sediments and high to very high conducting massive sulphides that meet the envisioned application of the MARTEMIS system. To calibrate the synthetic biased measurements ( $S_{WS,biased}$ ), an unbiased system response ( $S_{WS,unbiased}$ ) for a whole space (WS) of known conductivity is needed. This can be derived either from the 3D model

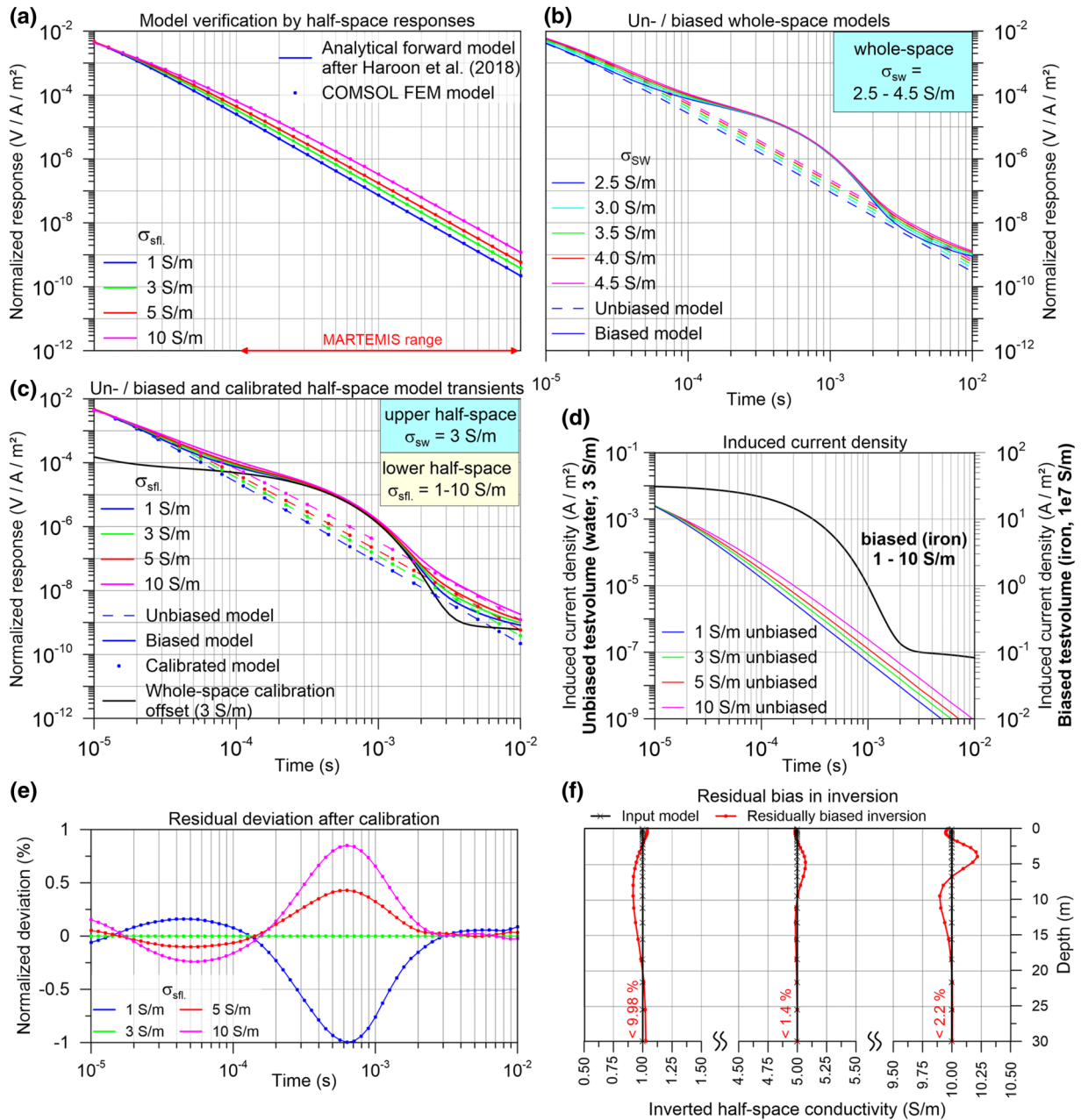


**Figure 4** Results of TDEM modelling: (a) TDEM verification of the FE model-derived solution against an analytical calculated forward model for varying lower half-space conductivities. (b) Unbiased (dashed, coloured) and biased (solid, coloured) transients of the MARTEMIS system for a set of whole-space conductivities ranging between 2.5 and 4.5 S/m. (c) Unbiased (dashed, coloured) versus biased (solid, coloured) model responses for a set of varying lower half-space conductivities with 1, 3, 5 and 10 S/m. Subtraction of the unbiased whole-space (3 S/m) response from the biased whole-space response results in the whole-space calibration offset (solid, black). This offset is used to calibrate all half-space responses (dots, coloured). (d) Induced current density in the defined testvolume of a single iron weight with different material properties (water, iron). In case of the testvolume being iron, a dependence of the current density on the lower half-space conductivities is no longer visible. (e) The deviation between the calibrated and unbiased model responses after the calibration is considered as residual bias. (f) Inversion of these residually biased half-space model responses. The input model was used as a starting model to avoid any Occam-related deviations ( $RMS \leq 1$ , error floor 1%). Due to the calibration the whole-space (3 S/m) response is perfectly calibrated while the 1, 5 and 10 S/m responses are showing equivalent variations to the signal deviation in (e) of up to  $\pm 1\%$  from the original signal in MARTEMIS' significant time range of  $10^{-4}$  to  $10^{-2}$  s. This leads to errors of up to  $\sim 10\%$  for a non-conductive seafloor with 1 S/m, whereas higher conducting seafloor show lower offsets of  $\sim 1.4\%$  for 5 S/m and 2.2% for 10 S/m. This favours the envisioned application of the MARTEMIS system targeting highly conductive ore deposits.



or more easily from an available, time-saving, analytical solution. By subtraction, a time-dependent calibration offset  $\Delta S$  is calculated (equation 10):

$$\Delta S(t) = S_{WS, \text{biased}} - S_{WS, \text{unbiased}} \quad (10)$$

This whole-space calibration offset is now subtracted from each biased transient, independently from the sub-seafloor conductivity, to obtain the calibrated transients (Fig. 4c, coloured point markers). The analysis of the resulting ‘calibrated’ signal shows similar transients compared with the unbiased signal, thus proving the general applicability of the concept.

### Residual bias in calibrated data

Normalization of this calibrated response to the unbiased signal for all seafloor measurements shows deviations less than 0.5% for most of the time series, but  $\sim 1\%$  in the time range of  $10^{-4}$  to  $10^{-3}$  s, which is in the magnitude of the expected minimum relative measurement error (Fig. 4e). Still, this additional error source stacks with systematic and random errors and may influence the retrieved conductivity of the data set. A considerable relevance to an inversion result can be attributed, since the sign of the deviation is dependent on the conductivity contrast: in the time range of  $10^{-4}$  to  $10^{-3}$  s, lower conductive half-spaces will produce negative deviations from the unbiased signal and vice versa. For the range of  $10^{-5}$  to  $10^{-4}$  s, a sign change with lower amplitude can be observed. However, since this time range is not resolvable by the MARTEMIS system, it is reasonable to deduce that the calibration will amplify the measured conductivity contrast towards seawater.

### Influence of residual bias on inversion results

To quantify this residual influence, the calibrated responses of the biased half-space models were inverted for the time range of  $10^{-4}$  to  $10^{-2}$  s, using an Occam-inversion algorithm (Constable *et al.*, 1987) based on the 1D forward code of Swidinsky *et al.* (2012). To avoid any Occam-based deviations, the input model was used as starting model for the inversion. Figure 4(f) shows the inversion results for each residually biased half-space model after calibration. Comparable to the normalized deviations of the calibrated model responses in Fig. 4(e), small variations are visible that depend on the conductivity of the lower half-space: the 1 S/m half-space exhibits the highest deviation by  $\sim 10\%$  at a depth span of 5 to 15 m. The conductive half-spaces 5 and 10 S/m show deviations of  $< 2.5\%$  in the range of 0 to 10 m, respectively.

Generally, the conductivity contrast is amplified as observed before: lower conductivities appear slightly less conductive, while higher conductivities appear more conductive. While for the uppermost part of the profiles, the start of the observed sign change can be recognized, the deeper part of the profile remains almost unbiased. Depending on the purpose of the instrument, this may influence the requested sensitivity of the sensor. In MARTEMIS’ case, of which purpose is to detect large, inactive massive sulphide deposits with high conductivities above seawater (3 S/m), a 2.5% deviation still results in the identification of the deposit. Thus, no severe consequences arise from this slight loss of sensitivity.

### System optimization to reduce residual bias

An optimization of the MARTEMIS system solely relates to the reduction of conductive elements in proximity of the coincident transmitter and receiver coils. In 2018, the metal weights were simply replaced by non-conductive barite weights and the metal edges by fibreglass composites, which proved to be extremely durable during recent measurements. Thus, conductive parts are completely eliminated from the lower frame and whole-space measurements are now in excellent agreement to the theoretical response.

## RESULTS FREQUENCY-DOMAIN

### Verification of 3D finite element model by 1D analytical forward model

Comparing the finite element (FE) model responses against the 1D analytical solution shows the successful development of the 3D FE model. To illustrate this in Fig. 5, the whole-space response is subtracted from each half-space response and displayed on a logarithmic scale: an excellent agreement is visible. Both the response based on the calculated induced voltage in the receiver (RX) coil ( $V_{\text{ind}, \text{RX}}$ ), as well as the solution based on vertical magnetic flux density derived from the central point probe ( $B_z$ ) show identical solutions. Due to the lower computational costs, the latter solution is used in all further calculations.

### Introduction of the bias effect in 3D finite element model

The results of the frequency-domain whole-space model show an effect similar to the one observed in the whole-space measurements of the INDEX2015 survey (cf. Fig. 2b). Especially the large titanium housings of the additionally carried

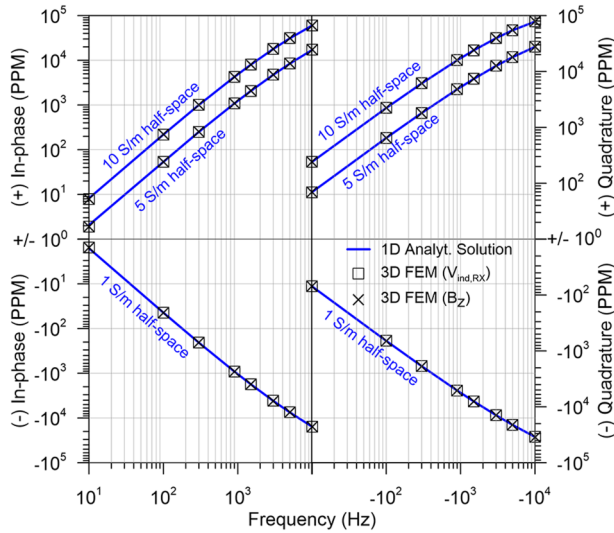


**Figure 5** FDEM verification; FDEM verification between the 3D FE models and the 1D analytical solution for a set of relative half-space responses of 1, 5 and 10 S/m: the whole-space response of 3 S/m is subtracted and a positive/negative logarithmic scale is used to allow for a better comparison. The signal of the induced voltage in the coil corresponds to the signal of the  $B_z$  component in the centre point of the coil (point probe), allowing for a simplification of the model and reducing computational time.

self-potential/induced polarization (SP/IP) system results in a major deviation from the initial configuration (Fig. 6a). The bias of an added pressure housing differs by (a) the in-phase or quadrature component, (b) the chosen frequency and (c) the conductivity of the surrounding whole space. Configuration A, yielding the basic set-up of GOLDEN EYE with two smaller electromagnetic housings to perform controlled-source electromagnetic method measurements, leads to a bias of approximately 50% in the low-frequency in-phase component and 2.5% in the low-frequency quadrature component, both decreasing towards higher frequencies. The influence of the conductivity is related to the conductivity contrast between seawater and the pressure housings. The bias increases with higher contrasts and therefore lower conductivities.

Configuration B, which adds two additional, larger pressure housings to the system for SP/IP measurements, multiplies the bias effect by a factor of 16, while the overall characteristics remain constant. Considering the pure titanium volume of the housings, which yields about  $6300 \text{ cm}^3$  for configuration A and approximately a threefold volume for configuration B, this effect does not simply scale with the pure titanium mass. It is more likely connected to the overall distribution of titanium between the TX and RX coils. The housings in configuration

A are 20 cm shorter than the added housings in configuration B and are placed further to the outside of the frame (see Fig. 6c for size reference).

### Calibration of biased data by 1D analytical forward model

To eliminate the bias without the removal of the necessary housings, calibration techniques are required. One of the applied techniques is based on the dependency between conductivity and observed response (Fig. 2b): a frequency- and phase (respectively in-phase/quadrature)- specific calibration against the forward-calculated (predicted) response is commonly used to eliminate system-immanent deviations between the analytical model and measured data to allow the inversion of the data. As shown by Müller *et al.* (2012) and Baasch *et al.* (2015), this can be achieved by the measurement of the seawater's conductivity via conductivity/temperature/depth probes during a survey, used to create a database of (biased) whole-space measurements ( $S_{\text{Biased}}$ ) and corresponding forward-calculated analytical solutions ( $S_{\text{CTD}}$ ) for the span of measured seawater conductivities (equation 11). By linear regression, a complex frequency ( $f$ )-dependent multiplier ( $A$ ) and offset value ( $B$ ) are calculated and used to calibrate the data set afterwards:

$$S_{\text{biased}}(f) = A(f) S_{\text{CTD}}(f) + B(f). \quad (11)$$

Limitations of the procedure arise from the fact that an optimum sensor calibration is achievable only when the conductivity of the surrounding is known and homogeneous. The true conductivity of the seafloor is generally unknown and may deviate in a large range of  $< 0.1 \text{ S/m}$  for resistive rocks like basalts to over  $10 \text{ S/m}$  for highly conducting ore deposits.

### Residual bias in calibrated data

Comparable to the time-domain electromagnetic evaluation, we examine the residual bias effects by the variation of the lower half-space's conductivity (0.1, 1, 5 and 10 S/m) in the model while calibrating the response with a whole-space measurement of 3 S/m. Figure 6(b) illustrates the residual bias as a surface in a conductivity-frequency space (red surface). The overall bias is effectively reduced by the calibration up to zero where the 3 S/m whole-space conductivity is reached. Deviating from this line, a residual bias remains for all other conductivities. For the in-phase components, the initial effect in the uncalibrated data is reduced drastically to  $\sim 1\%$ , showing a decrease towards a sign change

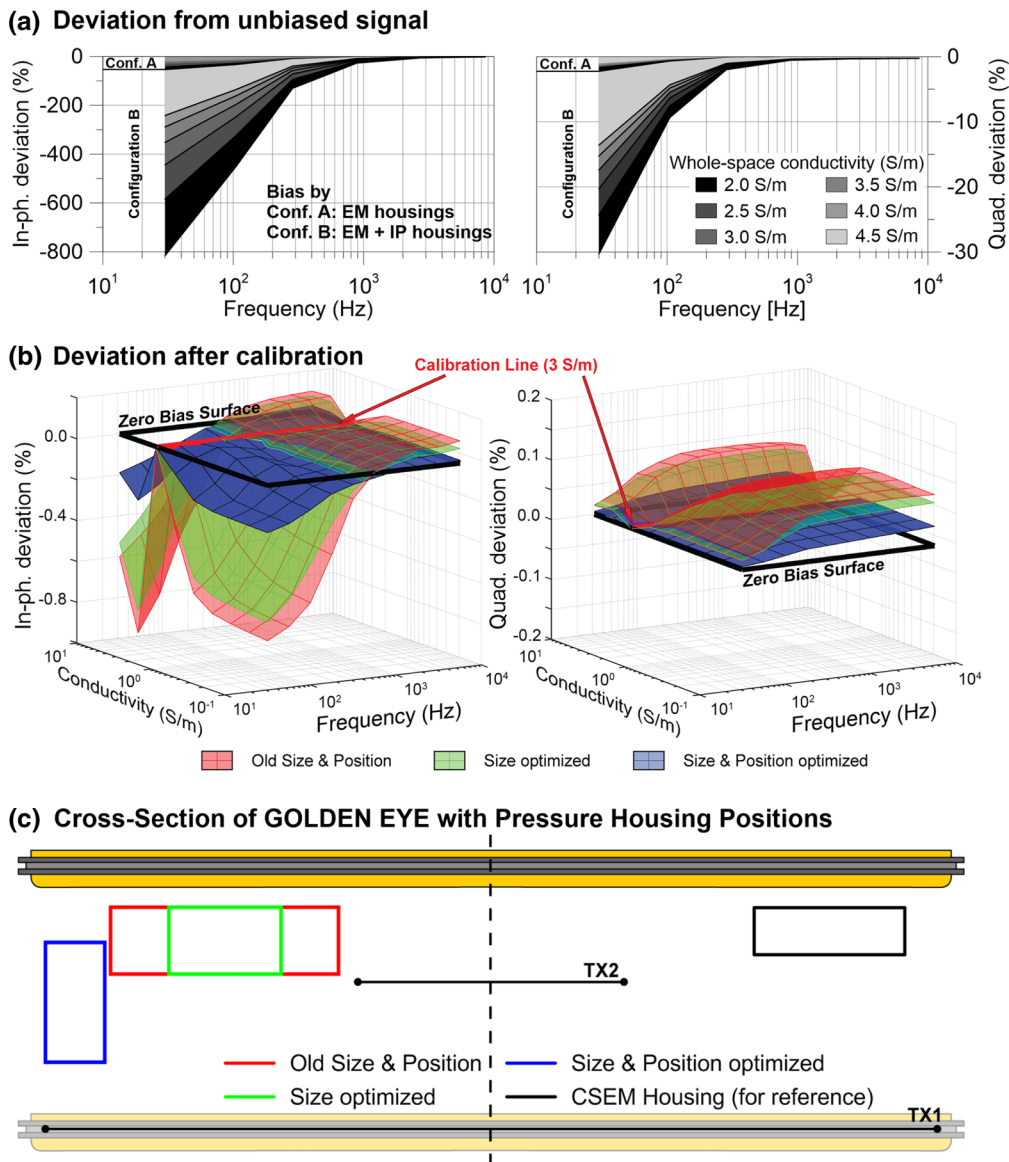


**Figure 6** FDEM bias and calibration of the GOLDEN EYE. (a) Deviation from the unbiased whole-space signals for a set of different whole-space conductivities and the two configurations of the device used during the INDEX2015 cruise. Configuration A represents the GOLDEN EYE minimal set-up with two (smaller) titanium housings used for the EM soundings. Configuration B includes the SP/IP system, represented by two additional, significantly larger titanium pressure housings. Thus, the bias effect is significantly larger. (b) Results of the system calibration as residual bias surfaces in a conductivity–frequency–space for the initial set-up (red) and two optimization steps (green, blue). The reduction of size (green) and the repositioning of the housing (blue) significantly reduce the amount of residual bias. The zero-bias-calibration line for 3 S/m is indicated as red line, while the optimum zero-bias-surface is illustrated in black. (c) Cross-section of the GOLDEN EYE indicating the different set-ups during the optimization process. The black box illustrates the size of one of the EM housings for reference needed to operate the system.

in the mid-frequency range and then rising up to 0.1% for the high frequencies. The quadrature component shows an equivalent reduction  $\sim 0.1\%$  decreasing further towards lower frequencies.

**System optimization to reduce residual bias**

With these results, approaches for a system optimization were gathered, leading to (a) a possible reduction in size of the pressure housings and (b) the resulting possibility to shift the

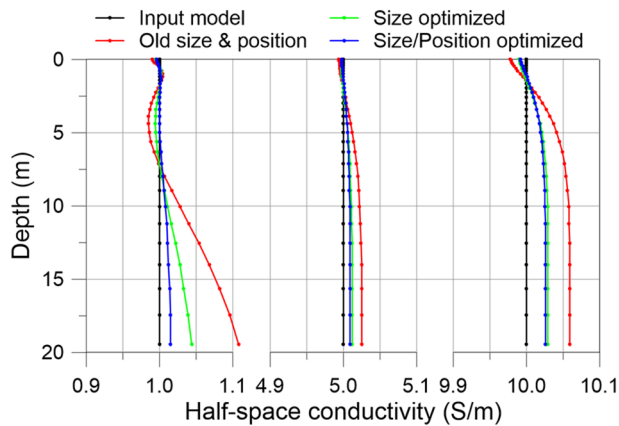


**Figure 7** Influence of residual bias on the inversion; 1D Inversion results of the residually biased half-space responses of 1, 5 and 10 S/m ( $RMS \leq 1$ ). Comparable with the TDEM results, the un-optimized deviation is highest for the lowest conductivity by  $\sim 10\%$  (0.1 S/m), followed by the 10 S/m response by  $\sim 0.6\%$  (0.6 S/m). Due to the lowest conductivity contrast towards the calibration point of 3 S/m, the 5 S/m response yields the lowest relative deviation of  $\sim 0.4\%$  (0.25 S/m). The system optimization reduces the maximum bias to 1% (1 S/m), 0.02% (5 S/m) and 0.025% (10 S/m).

position of the pressure housings to an optimum position (Fig. 6c). While option (a) targets the overall titanium mass in the configuration, option (b) relates to the geometric distribution of the titanium in relation to the coils. Both the size reduction (green surface) and repositioning, by rotating the housing by  $90^\circ$  and moving it as far away from the RX as possible (blue surface), effectively leads to a further reduction of the bias (Fig. 6b), while the general characteristics of the bias surfaces remain.

#### Influence of residual bias on inversion results

To assess the influence of the initial bias and the optimization steps on the inversion process, the residually biased signal of each step is inverted by an analytical 1D forward model-driven inversion routine (Baasch *et al.*, 2015). Corresponding to the higher penetrating low-frequency in-phase component, the deviation from the initial forward response is highest with  $>10\%$  for the highest penetration depths of 20 m, but also dependent on the half-space's conductivity (Fig. 7, red line). Here the higher conducting half-spaces show lower deviations of 0.5% (5 S/m) respectively 6% (10 S/m), emphasizing higher conducting targets. Following the results of the residual bias calculations, the optimization steps lead to a significant improvement of the inversion results by reducing the deviations for the low conductive half-space by  $\sim 90\%$  and for the higher

conducting half-spaces by approximately 50% (Fig. 7, blue and green line).

## DISCUSSION

The proposed calibration procedure yields an adequate approach to remove the larger part of the platform-immanent bias. We have shown that the remaining, residual bias is small enough to successfully invert the data and to produce reasonable results even though deviations remain. Whether these residuals are acceptable mainly depends on the envisioned application, sensitivity and resolution requirements of a device. For both MARTEMIS and GOLDEN EYE, a residual uncertainty of 1% to 2% for higher conducting cases, respectively,  $\leq 0.1$  to 0.2 S/m is rather negligible, considering the extremely inhomogeneous structure with large conductivity contrasts of a massive sulphide deposit. In comparison, a surficial sediment mapping device, like the NERIDIS benthic profiler with a smaller, comparable sensor to the GOLDEN EYE (Müller *et al.*, 2012), would suffer severely from similar bias offsets.

Nonetheless, some persistent issues need to be addressed. The most obvious is the loss of sensitivity by using an approximation to calibrate the data. Considering the maximum deviation of the biased signals after calibration of about 1% (Figs 4e and 6b), this systematic yet unknown error in terms of amplitude and sign stacks with the random noise level of the instrument, leading to an approximate twofold of the uncertainty. When respecting this larger error floor during the inversion by normalizing the data to this increased error, conductivity contrasts are harder to resolve and sensitivity is lost. However, disregarding this error will lead to the systematic over- or underestimation of the seafloor conductivity. In time domain, even an enhancement of the measured contrast can be predicted in the relevant time range, caused by the amplification of this effect (Fig. 4e and f). On the other hand, dynamic variations of this bias caused by moving conductive system components due to structural weaknesses during a survey will produce unpredictable time-dependent anomalies that are impossible to calibrate by the proposed method. While for static seafloor measurements this effect may be eliminated by landing the device, a possible ship-induced heaving motion in the water column during the calibration measurements or a more efficient flying mode close to the seafloor is problematic. At this point, the importance of the calibration measurements during the survey has to be stressed. The measurement of a known environment is required, which basically reduces the possible calibration points to the water column of known conductivity and sufficient extent that exceeds the depth of

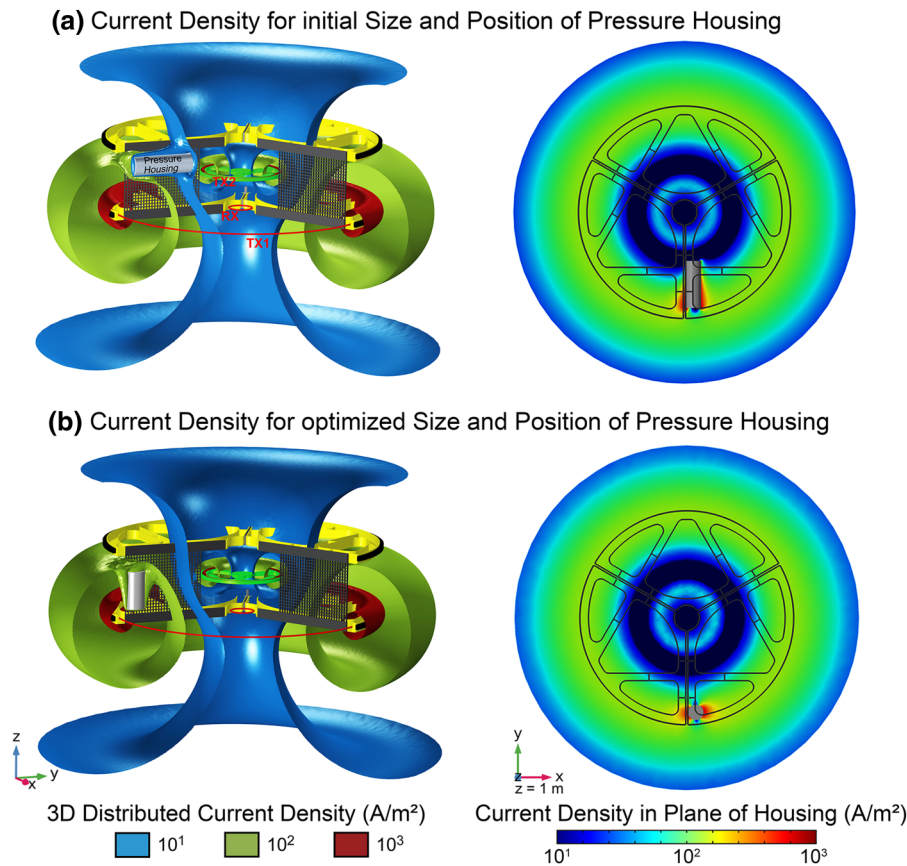


**Figure 8** Distortion of the generated ring current as 3D cut-away diagram (left) and horizontal plane view (right) in frequency domain (1000 Hz). (a) Deformation of the induced current density near the initially used titanium pressure housing. The induced ring current is channelled towards the higher conducting object as path of lowest resistance which forms local extrema. (b) The deformation of the induced current density is reduced due to the optimization of the pressure housing by resizing it and rotating it into a vertical orientation.

investigations (DOI) of the instrument. Strong thermohaline layering of the water column can be detected by conductivity/temperature/depth measurements during the diving phases and needs to be respected by a layered forward model in processing. Time-varying layering in coastal areas needs to be countered by multiple calibration points, covering the complete survey. Too sparse calibration points that hardly cover the range of upper half-space conductivities during seafloor measurements, as well as bias sources in range (e.g. ships), will lead to offsets and an invalid calibration. This usually results in the systematic over- or underestimation of the inverted conductivity section. Therefore, a practical way to deal with calibration measurements is to include them at each start and end of a profile, leading to a large database of calibration points that can handle occasional imprecise measurements as well as seawater conductivity variations and drift effects.

Considering these limitations, optimized platforms are the way forward to keep the immanent bias as low as pos-

sible for cases when metallic components are not completely inevitable. Here, the optimization procedure for the GOLDEN EYE showcased an important aspect: the signature of metallic components is not solely related to the inductive coupling and thus does not simply scale with the amount of conductive material used. It is also affected by the channelling of the generated ring current through the higher conducting object, leading to a conductive coupling effect that influences the geometrical distribution of the secondary fields and ultimately the measured response. While the inductive effect is related to the volume of conductive material and the magnetic flux density as a function of distance to the source, the conductive effect can be attributed to the geometrical distribution of the conductive material near the sensor. The placement of the metallic pressure housings in areas of steep E-field gradients leads to the production of large, local extrema due to the current channelling, and thus high offsets in the measured signal (Fig. 8a). Moving the housing to a more homogeneous area results in

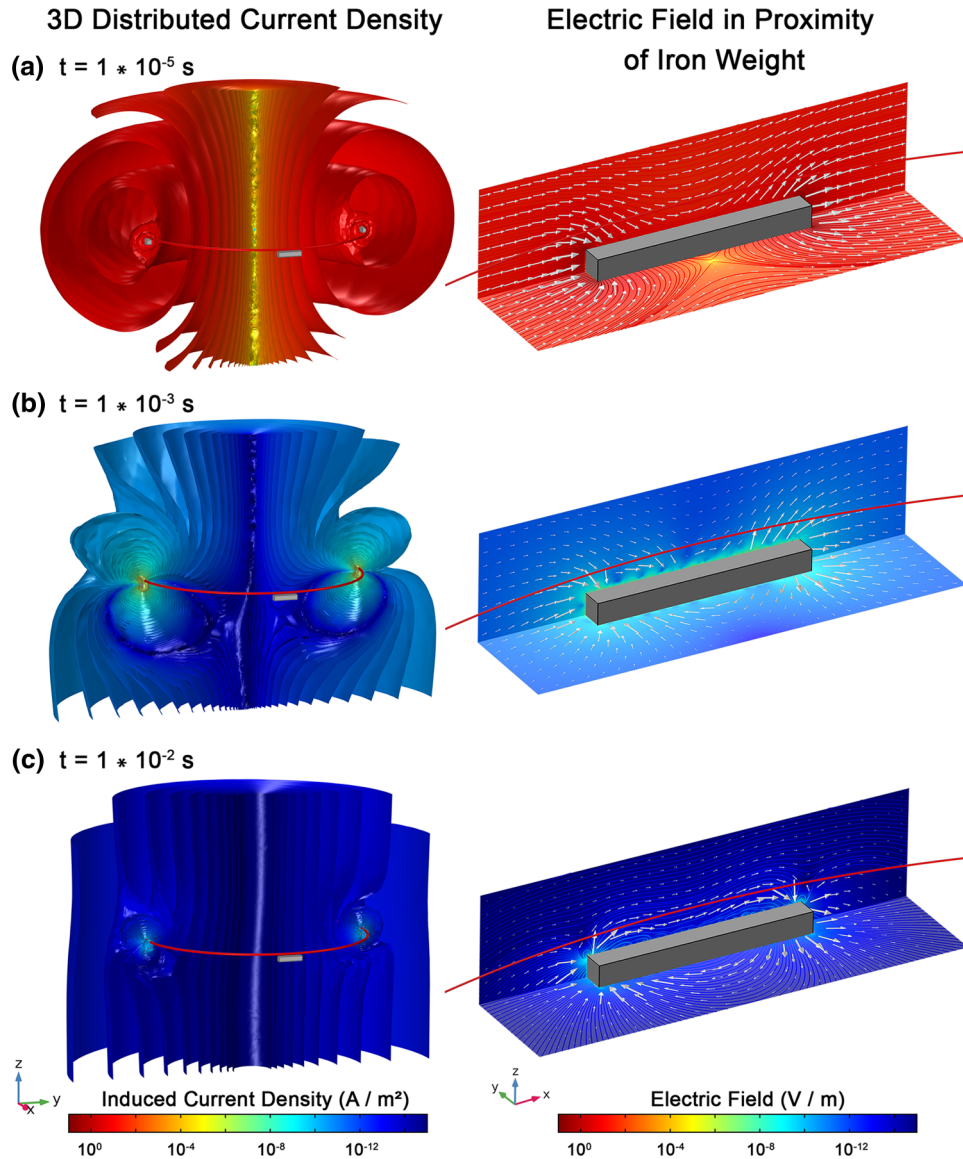


**Figure 9** Distortion of the generated current density as 3D cut-away diagram (left) and the distribution of the electric field near the iron weights (right) in time domain. At  $10^{-6}$  s, (a) the current density distribution (left) is essentially dominated by the induced ring current, which leads to a channelling of the electric field through the higher conducting body and the charge up of the weight (right). Subsequently and represented by  $10^{-3}$  s (b) and  $10^{-2}$  s (c), the charged-up weights start to produce secondary, dipole-like fields (right), which lead to the distortion of the current density (left). Note that the central area of the coil still shows a homogeneous current density distribution.

smaller local extrema with less influence on the measured signal, even though the inductive effect may increase (Fig. 8b). However, the repositioning of a housing into areas of low field gradients away from the sensitive receiver (RX) will reduce the inductive effect and may be considered if compactness is not required.

In the time-domain case, the same effects are visible in early times but now also relate to the decaying induced

ring current. At  $10^{-5}$  s, the channelling of the ring current through the conductive object is visible and comparable to the frequency-domain electromagnetic case, leading to the observed increase of the induced current density, indicating the charge up of the object (Fig. 9a). In the surrounding volume, the generated ring current still dominates, while no offset is visible in the signal. Subsequently, the distributed current density starts to change significantly. The charged up weights

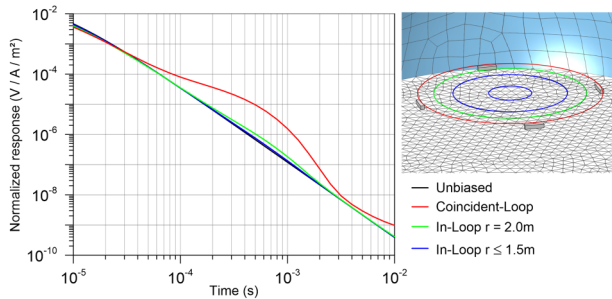


**Figure 10** Comparison between coincident-loop and in-loop responses in time domain. Biased whole-space responses are calculated for different in-loop RX configurations. Due to the less distorted centre area of the coil, smaller RX areas show a lower bias, even though no further improvements are visible below a radius of 1.5 m.

produce local, dipole-like anomalies by the slower decaying charge that distorts the decaying ring current and, thus, the signal (Fig. 9b). This effect is dominant up to  $5 \times 10^{-3}$  s when the secondary fields start to decrease and the current density distribution normalizes (Fig. 9c).

Even though the effect was removed for the MARTEMIS system by replacing the weights and edges with non-conductive materials, we can propose an optimization strategy for more complex cases where this may not be feasible. Considering AUVs, ROVs or any other dedicated multi-sensor platform, it is unlikely to replace or move initially mounted instruments and parts in favour of the controlled-source electromagnetic method (CSEM) sensor. Nakayama and Saito (2016) discussed and tested two additional configurations to avoid noise in their measured data, by separating the remotely operated vehicle from the sensor, using a towed system and using their CSEM sensor as a deployable station. Another common approach would certainly be to separate the RX from the disturbed near field in proximity of the transmitter (TX), by moving it to the undisturbed far field. Still these options drastically increase costs and efforts while sacrificing the compactness of the device. Another remaining, more elegant optimization approach is therefore to modify the TX/receiver (RX) geometry by avoiding distorted field areas in the integration area of the coil. Hence, we can utilize the more homogeneous field distribution, found towards the centre of the MARTEMIS system, avoiding the local anomalies in proximity of the TX coil (Fig. 9). Accordingly, this would translate into changing from a coincident loop to a central in-loop configuration with a smaller RX radius. To test this approach in our model, we reduced the RX radius stepwise, to analyse the effect on the bias in a 3 S/m whole-space environment (Fig. 10). We found that an in-loop RX radius of 1.5 m reduces the bias to a minimum.

A further decrease to 0.5 m does not yield any further improvement. While a calibration is still necessary for this case, the lower bias will lead to a numerically more stable offset calculation. The difference between the biased and unbiased response becomes smaller and the influence of imprecise calibration measurements decreases. However, possible drawbacks of a smaller RX coil in terms of a lower signal-to-noise ratio and thus a lower DOI need consideration, as well as the structural more complex set-up.

## CONCLUSION

The observed bias effects in marine controlled-source electromagnetic method (CSEM) data have been successfully re-traced to conductive objects in close proximity to the receiver (RX) for both time- and frequency-domain cases. Numerical modelling showed how highly conducting metal components change the response as a function of the surrounding seawater and seafloor conductivity. A primary calibration of the measured data against the predicted response of the measured seawater conductivity can be considered as a valid approach to remove a substantial part of the bias for both time and frequency domain, enabling an inversion of the data and producing reasonable results. However, a residual bias remains as a function of seafloor conductivity and time respectively frequency. In our numerical case studies, we detected maximum bias levels of 1% to 2% after calibration, approximately doubling the estimated uncertainty of the devices. After inverting this calibrated data, this accounts for 0.1 to 0.2 S/m deviation. For higher conductivities and conductivity contrasts towards the background material, these values become increasingly negligible, favouring the intended usage in ore deposit exploration. Since the seafloor conductivity is generally not known, but the objective of the inversion process, this residual bias cannot be removed by calibration procedures without significant effort (e.g. ground truthing). For these cases, optimization approaches yield the possibility of a further reduction of this platform-immanent bias. Redesigning and repositioning essential conductive system components into bias-minima results in less disturbance of the distributed current density at the RX coil. Hence, we regard this as the way forward to remove a considerable part of the platform-immanent bias, and to design and build compact, multi-sensor platforms including CSEM sensors without sacrificing too much of the sensor's sensitivity. At this point, a careful evaluation between the benefits and the impact of additional sensors and devices needs to be carried out since every conductive component still increases the immanent bias level. In case of existing

designs, especially considering autonomous unmanned vehicle/remotely operated vehicle-based solutions, the modification of the transmitter/RX geometry (e.g. changing from coincident loop to in-loop) may offer an elegant approach to reduce bias without changing the platform itself. In either case, sensitivity investigations and optimization strategies should be carefully evaluated, taking advantage of the recent developments in 3D finite element simulation.

#### AVAILABILITY OF DATA AND MATERIALS

Data sharing is not applicable to this article as no new data were created or analysed.

#### DECLARATIONS


All the authors declare that they have no competing interests and that they have approved the manuscript for submission. The manuscript has not been published or submitted for publication elsewhere.


#### ACKNOWLEDGEMENTS

The authors would like to thank Martin Wollatz-Vogt (GEOMAR) for the technical support of the MARTEMIS system, Christian Hilgenfeldt (MARUM), Tilo von Dobeneck and the marine geophysics group of the University of Bremen for the ongoing support over the last years. Further, we would like to thank Andrei Swidinsky (Colorado School of Mines) for his useful remarks. This work was partly funded by the Federal Institute for Geosciences and Natural Resources (BGR) for the development and improvement of the GOLDEN EYE CSEM profiler. Further funding was received by the German Research Foundation (DFG) as part of the Project No. 366335859 (HO 5236/1-1), including geophysical and geological investigations at the Palinuro Seamount off Sicily as well as the ongoing development and operation of the MARTEMIS system. In addition, work was also supported in the scope of the project 'Gitaro.JIM' (03SX456C) by the German Federal Ministry for Economic Affairs and Energy and co-funded by European Union's Horizon 2020 research and innovation programme under the framework of ERA-NET Cofund MarTERA (Maritime and Marine Technologies for a new Era).

#### ORCID

Konstantin Reeck  <https://orcid.org/0000-0002-0187-0863>

Amir Haroon  <https://orcid.org/0000-0001-5138-6730>

Katrin Schwalenberg  <https://orcid.org/0000-0002-0511-6075>

#### REFERENCES

- Baasch, B., Müller, H., Oberle, F.K. and von Dobeneck, T. (2015) Inversion of marine multifrequency electromagnetic profiling data: a new approach to resolve surficial sediment stratification. *Geophysical Journal International*, 200, 439–451.
- Bloomer, S., Kowalczyk, M., Kowalczyk, P., Constable, S., Haber, E. and Kasuga, T. (2018) *AUV-CSEM: An Improvement in the Efficiency of Multi-sensor Mapping of Seafloor Massive Sulfide (SMS) Deposits with an AUV*. Kobe, Japan: IEEE Oceans.
- Cairns, G.W., Evans, R.L. and Edwards, R.N. (1996) A time domain electromagnetic survey of the TAG hydrothermal mound. *Geophysical Research Letters*, 23, 3455–3458.
- COMSOL AB (2017) COMSOL Multiphysics Reference Manual, available at: [www.comsol.com](http://www.comsol.com), last accessed: 4 Mar 2020.
- Constable, S., Parker, R.L. and Constable, C. (1987) Occam's inversion: a practical algorithm for generating smooth models from electromagnetic sounding data. *Geophysics*, 52(3), 289–300.
- Gehrmann, R.A.S., North, L.J., Graber, S., Sztikar, F., Petersen, S., Minshull, T.A. *et al.* (2019) Marine mineral exploration with controlled source electromagnetics at the TAG hydrothermal field, 26°N Mid-Atlantic Ridge. *Geophysical Research Letters*, 46, 5808–5816.
- Haroon, A., Hölz, S., Gehrmann, R.A.S., Attias, E., Jegen, M., Minshull, T.A. *et al.* (2018) Marine dipole-dipole controlled source electromagnetic and coincident-loop transient electromagnetic experiments to detect seafloor massive sulphides: effects of three-dimensional bathymetry. *Geophysical Journal International*, 215, 2156–2171.
- Hölz, S. (2017) *RV POSEIDON Fahrtbericht/Cruise Report POS509 - ElectroPal 2: Geophysical investigations of sediment hosted massive sulfide deposits on the Palinuro Volcanic Complex in the Tyrrhenian Sea, Malaga (Spain) - Catania (Italy) 15.02.-03.03.2017*, GEOMAR Report, N. Ser. 039. Germany: GEOMAR Helmholtz-Centre for oceanic research Kiel.
- Hölz, S., Haroon, A., Reeck, K. and Jegen, M. (2018) MARTEMIS – A New EM Tool for the Detection of Buried Seafloor Massive Sulfides, 24th International EM Induction Workshop, Helsingør, Denmark.
- Hölz, S., Jegen, M., Petersen, S. and Hannington, M.D. (2015) How to find buried and inactive seafloor massive sulfides using transient electromagnetics: a case study from the Palinuro Seamount in the Tyrrhenian Sea. Underwater Mining Conference.
- Ishizu, K., Goto, T., Ohta, Y., Kasaya, T., Iwamoto, H., Vachiratienchai, C. *et al.* (2019) Internal structure of a seafloor massive sulfide deposit by electrical resistivity tomography, Okinawa Trough. *Geophysical Research Letters*, 46(20), 492.
- Kowalczyk, P. (2008) Geophysical prelude to first exploitation of submarine massive sulphides. *First Break*, 26, 99–106.
- Lee, S.K., Ko, H., Park, I.H., Cho, S.-J., Won, I.J., Funak, F. *et al.* (2016) *Experiment and Response Analysis of Marine Monostatic*



- EM Instrument Toward Mapping Seafloor Sulfide Massive Deposit*. Shanghai, China: IEEE Oceans 2016.
- Müller, H., Schwalenberg, K., Reeck, K., Barckhausen, U., Schwarz-Schampera, U., Hilgenfeldt, C. *et al.* (2018) Mapping seafloor massive sulfides with the golden eye frequency-domain EM profiler. *First Break*, 36, 61–67.
- Müller, H., von Dobeneck, T., SanFilipo, B., Hilgenfeldt, C., Rey, D. and Rubio, B. (2012) Mapping the magnetic susceptibility and electric conductivity of marine surficial sediments by benthic EM profiling. *Geophysics*, 77(1), E43–E56.
- Nakayama, K. and Saito, A. (2016) *Practical Marine TDEM Systems Using ROV for the Ocean Bottom Hydrothermal Deposits*. Kobe, Japan: IEEE Techno-Ocean.
- Schwalenberg, K., Müller, H. and Engels, M. (2016) Seafloor Massive Sulfide Exploration – A New Field of Activity for Marine Electromagnetics. EAGE/DGG Workshop on Deep Mineral Exploration, Extended Abstracts.
- Swidinsky, A., Hölz, H. and Jegen, M. (2012) On mapping seafloor mineral deposits with central loop transient electromagnetics. *Geophysics*, 77, E171–E184.
- Von Herzen, R.P., Kirklin, J. and Becker, K. (1996) Geoelectrical measurements at the TAG hydrothermal mound. *Geophysical Research Letters*, 23, 3451–3454.
- Ward, S.H. and Hohmann, G.W. (1988) Electromagnetic theory for geophysical applications. In: Nabighian, M.N. (ed.) *Electromagnetic Methods in Applied Geophysics*. Society of Exploration Geophysicists, pp. 130–311.
- Won, I.J., Keiswetter, D.A., Hanson, D.R., Novikova, E. and Hall, T.M. (1997) GEM-3: a monostatic broadband electromagnetic induction sensor. *Journal of Environmental and Engineering Geophysics*, 2(1), 53–64.